Astrophys Space Sci (2018) 363:266
https://doi.org/10.1007/s10509-018-3476-x

ORIGINAL ARTICLE

Predicting short-term $F_{10.7}$ with transport models

Cheng-ao Liu[1,2] · Xin-hua Zhao[1] · Tao Chen[1] · Hui-chao Li[1,2]

Received: 13 June 2018 / Accepted: 21 November 2018

Abstract A solar magnetic flux transport model has the ability to demonstrate the magnetic evolution of the Sun, thus providing a foundation for space weather forecasting. Solar activities have close relationships to the Sun's magnetic fields. To predict the Sun's magnetic environment more precisely, many versions of magnetic flux rope models have been developed. We utilized two models that were created by Yeates et al. (Sol. Phys. 245(1):87, 2007) (hereinafter referred to as the Y model) and Worden and Harvey (Sol. Phys. 195(2):247, 2000) (hereinafter referred to as the WH model) to predict the short-term changes of 10.7 cm radio flux ($F_{10.7}$) during 2003–2014. Both models performed very well in estimating $F_{10.7}$ values. The statistical results of analyzing the correlation coefficient, mean absolute error, mean square error, relative error, frequency distribution, etc. show that the Y model is superior to the WH model. The meridional flow and diffusion process used in the WH model do not agree with the observations. Such discrepancies may influence estimates of the global flux.

Keywords Solar magnetic fields · Flux transport model · $F_{10.7}$

✉ C.-a. Liu
caliu@spaceweather.ac.cn

X.-h. Zhao
xhzhao@spaceweather.ac.cn

[1] State Key Laboratory of Space Weather, National Space Science Center, Chinese Academy of Sciences, Beijing 100190, People's Republic of China

[2] University of Chinese Academy of Sciences, Beijing 100049, People's Republic of China

1 Introduction

Solar radio flux at 10.7 cm, abbreviated $F_{10.7}$, is an important index of solar activity. It has been measured by the Canada National Research Institute since 1947 (Tapping 2013; Svalgaard 2016). The source of the $F_{10.7}$ is mainly the upper layer of the chromosphere and the bottom of the corona. It has a close relationship with the active regions on the Sun. In addition, contributions to the formation mechanism of the $F_{10.7}$ include thermal free–free emission and thermal gyroresonance processes (Tapping and DeTracey 1990; Gary and Hurford 1987; Akhmedov et al. 1986). Free–free emission occurs all over the solar disc, and it is enhanced where the concentrations of plasma are high in the chromosphere and corona. Gyroresonance emission, on the other hand, takes place in the vicinity of sunspots where the magnetic fields are sufficiently strong. $F_{10.7}$ is easier to measure and unaffected by the weather on the Earth compared to other indices such as numbers of sunspots, extreme ultraviolet (EUV), ultraviolet (UV), and X-rays (Lampropoulos et al. 2016). It is often used as an input parameter to predict and reconstruct other electromagnetic radiations of the Sun. $F_{10.7}$ is generally thought to be a good proxy for the EUV and UV flux (Henney et al. 2015; Svalgaard 2016). Bilitza (2001) applied $F_{10.7}$ to study the variation of EUV, which can ionize and heat the Earth's upper atmosphere (Chen et al. 2018). Krivova et al. (2009) used the $F_{10.7}$ index to reconstruct the solar UV radiation series, which allows us to understand variations of the Earth's climate. Satellite operators are capable of predicting space–weather effects on satellites using $F_{10.7}$ (Ahluwalia 2016).

Many different methods have been developed to predict $F_{10.7}$. Chatterjee (2001) used the daily $F_{10.7}$ data during 1978–1988 to train an artificial neutral network (ANN) model. They used the model to predict the $F_{10.7}$ value 1 day

Published online: 12 December 2018

in advance during 1993. The results showed that the correlation coefficient between the observed and predicted values was 0.93. Huang et al. (2009) applied a method based on support vector regression (SVR) to forecast the short-term (days) values of the $F_{10.7}$. During the best year in 2006, the norm mean square errors (NMSE) were 2.71% and 4.48% for the 1-day and 3-day forecasts, respectively. During the worst year in 2003, they were 5.56% and 9.32%, respectively. Zhao and Han (2008) reconstructed the development history of $F_{10.7}$, and they put forward a new method for predicting the long-term (months–years) variations of solar 10.7 cm radio flux.

Chapman and Boyden (1986) used magnetograms obtained at the 150-foot tower telescope on Mount Wilson and divided them into weak and strong magnetic fields. The magnetic fields with absolute values between 10 G and 100 G were assumed to be facular (weak magnetic fields), and those greater than 100 G were assumed to be sunspot areas (strong magnetic fields). They modified the variations of the irradiance and compared them with measurements from the Active Cavity Radiometer Irradiance Monitor (ACRIM) from 1980 to 1984. The results showed that the decrease of solar irradiance during this period was caused by the decline of magnetic activity. Parker et al. (1998) adopted two similar indices, i.e., the Magnetic Plage Strange Index (MPSI) and the Mount Wilson Spot Index (MWSI). They modified solar UV and EUV irradiances and found a strong correlation between MPSI and $F_{10.7}$. Jain and Hasan (2004) used MWSI and MPSI to reconstruct the total solar irradiance of different solar cycles, and they found that variations of the total solar irradiance have a close relationship with the absolute magnetic-field strengths on the solar surface. Henney et al. (2012) found that the indices S_P and S_A are similar to MPSI and MWSI. We utilized two indices S_P and S_A, and two types of surface flux transport (SFT) models (Worden and Harvey 2000; Yeates et al. 2008) to modify the magnetic evolutions between 2003 and 2014. Based on the daily observed magnetic field, we forecasted photospheric magnetic maps for 1–3 days and then combined these with the empirical formula to predict $F_{10.7}$.

The magnetic field plays an important role in solar activities. The solar dynamo explains the basic rule of the magnetic activity, i.e., one part of the dynamo energy comes from the kinetic energy produced by solar rotation, and the other part comes from small-scale turbulence. In the interior of the Sun, the magnetic fields are driven by plasma motions. Because the rotation at the equator is faster than that at the pole regions, the magnetic fields are stretched and form toroidal fields (Hotta and Yokoyama 2010). This phenomenon is referred to as differential rotation. The small scale motions are associated with the Coriolis force. They twist the toroidal fields and generate the poloidal fields (Kosovichev 2009).

In the solar dynamo and the flux transport model, the meridional circulation cannot be neglected. On the surface of the Sun, materials from the equator are transported to the polar regions, while in the interior, there exists the equatorward return flow (Dikpati and Gilman 2009). The meridional flow is more difficult to observe because its velocity is an order of magnitude weaker than the differential rotation. On the surface, the velocity of the flow is approximately 10–20 m s^{-1}, while the flow in the interior becomes slower because of the increased density. According to the measurements of helioseismology, the velocity in the interior is approximately several meters per second (Kholikov et al. 2014).

The magnetic fields are also influenced by small-scale movements, such as the diffusion of supergranules. Leighton (1964) first proposed this concept, which represents the supergranules' dispersion effect on the photoshpere's magnetic fields. The results of Yeates et al. (2008) suggested that both the diffusion and the meridional flow play an important role in the reversion of the magnetic polarity in the polar area. Dikpati et al. (2006) used the low diffusion and high conversion model to predict that the strength of the magnetic flux in solar cycle 24 should be approximately 50% higher than that in cycle 23. In contrast, Choudhuri et al. (2007) used the high diffusion and low conversion model to predict that the activity of solar cycle 24 would be 35% weaker than that of cycle 23. The observation indicated that the magnetic behavior in solar cycle 24 was weaker than that in the previous cycle. The prediction of Choudhuri et al. (2007) is more suitable for the present situation, suggesting that diffusion cannot be ignored in the flux transport.

The structure of this paper is as follows. In Sect. 2, we illustrate the origin of the time series of $F_{10.7}$ and the magnetograms. In Sect. 3, we explain the conception of the solar surface flux transport model and how to use the magnetograms to predict $F_{10.7}$. The fitting results and discussions are given in Sect. 4. Finally, conclusions of this study are presented in Sect. 5.

2 Data

$F_{10.7}$ is given in solar flux units (1 sfu $= 10^{-22}$ W m^{-2} Hz^{-1}). The origin of $F_{10.7}$ is the chromosphere and the bottom of the corona. Daily $F_{10.7}$ observation data are downloaded from the site of Natural Resources Canada (http://www.spaceweather.gc.ca). Since the distance between the Sun and the Earth changes with time, the observed flux values are modulated. When used to compare with other solar activity indices, the modulation can be corrected by multiplying by the current Sun–Earth distance in astronomical units squared, which refers the flux values to a constant distance of 1 AU (Tapping 2013). This is called the Adjusted Flux.

In this paper, all values of the $F_{10.7}$ that we used are the Adjusted Flux.

Magnetic synoptic maps provide the magnetic field distributions on the photosphere. Though the method of observation and the precision of the instruments are improved continuously, the observed synoptic maps cannot estimate the solar magnetic field precisely for the following reasons: (i) traditional synoptic maps include data more than 13 days old and cannot display the true state of the photospheric magnetic field. (ii) The magnetic field on the Sun evolves continuously when we reconstruct the synoptic magnetograms. (iii) There are uncertainties in correcting the magnetic field at high latitudes. (iv) The polar regions cannot be observed because of the inclination between the Sun's equator and the ecliptic. (v) At present, we can observe only the Earth-side magnetic fields on the Sun; the lack of information from the back side of the Sun limits the precision of the synoptic maps (Virtanen et al. 2017; Worden and Harvey 2000; Henney et al. 2012). Historical observations have shown that there are large-scale movements on the solar surface, and the evolution of the magnetic flux follows the differential rotation and meridional flow processes. Furthermore, small-scale motions from supergranular cells contribute to the diffusion of the magnetic flux. Additionally, fluxes with different signs will converge when they encounter each other. The solar-surface flux transport model based on these rules can simulate the large-scale and long-term magnetic field's evolution process on the surface of the Sun (Baumann et al. 2004; Mackay and Yeates 2012). In this paper, we used the magnetic data from October 2003 to October 2014 and the SFT model to forecast $F_{10.7}$. The photospheric magnetic maps from October 2003 to May 2010 were obtained from the *Michelson Doppler Image* (*MDI*)/Solar and Heliospheric Observatory (SOHO) satellite's daily updated remapped images (http://soi.stanford.edu/data/). The maps from June 2010 to October 2014 were from the *Helioseismic and Magnetic Imager* (*HMI*)/Solar Dynamics Observatory (SDO) daily synoptic images (http://jsoc.stanford.edu/ajax/lookdata.html). Most magnetograms were available from those two satellites. If magnetograms were not available, we used the *Global Oscillation Network Group* (*GONG*) (https://gong.nso.edu/) or Carrington Rotation Synoptic Maps (http://sun.stanford.edu/synop/).

3 Method

The flux transport model utilizes photosphere magnetic-field data to evaluate the changing tendencies of the magnetic fields, especially in the data-poor or no-data areas, such as at the two poles and the far-side of the Sun. We used the Earth-side magnetic field distributions and divided them into two parts according to the absolute values of the radial magnetic fields. The daily observed radial magnetic magnetogram was input into the model. The input magnetogram was identical for these two models. When forecasting $F_{10.7}$ values, we still input the magnetogram into the SFT model to update the magnetic fields. According to Worden and Harvey (2000), the input images in the SFT model are flat maps with heliographic (latitude and longitude) coordinates. However, the original maps used x–y coordinates; therefore, we needed to transform the map from x–y coordinates to heliographic coordinates. The magnetic flux was added to the flat map by considering the transformation between the original map and the flat map. Then, we calculated a weight map as the sum of the number of pixels from the original map that overlapped pixels in the flat map. The flat map of the magnetic flux was normalized by the weight map. Because of the adjacent side effect and the inclination between the Sun's equator and the ecliptic, the measurement error increases from the solar disk center to the limb. We selected an area of 100 degrees in latitude and 130 degrees in longitude as the input map. Based on the magnetic field's distributions obtained from the predictions of the SFT model, we calculated the best-fitting coefficients in the empirical formula. Finally, the prediction of the $F_{10.7}$ could be realized using the empirical formula.

3.1 Surface flux transport model

Magnetic transport on the solar surface includes differential rotation, meridional flow, supergranule diffusion, and newly emerged flux. Both the WH and Y surface flux transport models contain these processes. In the Y model, the evolution of the radial magnetic field on the photosphere is given by Mackay and Yeates (2012):

$$\frac{\partial B_r}{\partial t} = -\Omega(\theta)\frac{\partial B_r}{\partial \phi} - \frac{1}{R\sin\theta}\frac{\partial}{\partial \theta}\left[u(\theta)B_r\sin\theta\right] + \frac{D}{R^2}\left[\frac{1}{\sin\theta}\frac{\partial}{\partial\theta}\left(\sin\theta\frac{\partial B_r}{\partial\theta}\right) + \frac{1}{\sin^2\theta}\frac{\partial^2 B_r}{\partial\phi^2}\right] + S \tag{1}$$

where, B_r is the radial magnetic field, R is the solar radius, θ is the colatitude, ϕ is the longitude, and t is time.

As shown in Snodgrass (1983), the differential rotation depends on the latitude as given by

$$\Omega(\theta) = 0.18 - 2.3\cos^2\theta - 1.62\cos^4\theta \ \text{deg day}^{-1}. \tag{2}$$

The meridional flow $u(\theta)$ is adopted from the profile of Yeates et al. (2007):

$$u(\theta) = C\cos\left[\frac{\pi(\theta_{\max} + \theta_{\min} - 2\theta)}{2(\theta_{\max} - \theta_{\min})}\right]\cos\theta \tag{3}$$

where, $\theta_{\min}$ and $\theta_{\max}$ are polar boundaries, the constant $C = -36\ \mathrm{m\,s^{-1}}$. The flow reaches its maximum of $16\ \mathrm{m\,s^{-1}}$ at mid-latitudes. The third term in (1) represents the magnetic flux diffusion caused by the convective motions of the supergranules, where the diffusion coefficient $D = 450\ \mathrm{km^2\,s^{-1}}$. The last term S is a source term, representing newly emerging sunspots. Since the magnetogram is input into the model daily, we need no additional information to represent the emerging magnetic fields, and we set $S = 0$ in our simulation.

The computational region was $[0, \pi] \times [0, 2\pi]$, and the resolution of the grid in the θ and ϕ directions was 1°. The flux transport model can be solved by the finite-difference method where the time step satisfies

$$\Delta t = \mathrm{CFL}\ \min\left(\frac{R\sin\theta\Delta\phi}{u_{\max}}, \frac{(R\sin\theta\Delta\phi)^2}{D}\right) \tag{4}$$

where CFL is the Courant number for which we choose CFL = 0.8 (Courant et al. 1967) and $u_{\max}$ is the maximum convection speed. In practice, considering the convergence of the grid at two poles, the computational region in the latitudinal direction was $5° \le \theta \le 175°$. The values at the poles were extrapolated and averaged by the values at $\theta = 5°$ or 175°.

The governing equation of the Y model was deduced from the induction equation. However, the WH model did not solve this equation. The WH model calculates the movements of the pixel produced by transport processes. Initially, a Carrington synoptic map was input into the WH model. Then, the pixel movements caused by the differential rotation, supergranular diffusion and meridional flow were calculated. Furthermore, to prevent the magnetic field decay of the quiet-Sun, Worden and Harvey (2000) added a Gaussian distribution magnetic flux with the mean absolute value of 1.8 G to the background. Finally, the daily observed magnetic fields were merged into the model.

The differential rotation used in the WH model was the same as that in the Y model; they both adopt the expression given by Snodgrass (1983). The meridional flow equation in the WH model is different from the Y model. The equation is as follows

$$M(\sigma) = 8|\sin\sigma|^{0.3}|\cos\sigma|^{0.1}\ \mathrm{m\,s^{-1}} \tag{5}$$

where M is the meridional flow and σ is the latitude. The peak flow was $7.2\ \mathrm{m\,s^{-1}}$ at the latitude of 30° in each hemisphere.

Because the sizes and the lifetimes of the supergranular cells are hard to measure, it is difficult to determine the diffusion processes. The supergranular cells randomly distribute on the quiet sun area. Unlike the Y model use of a coefficient, the WH model utilizes "random attractors" to represent the diffusion processes. First, an "attractor" matrix is created the same size as the synoptic map (360 × 180 pixels). Each pixel in the matrix is assigned a random number between 0 and 1. The WH model defines a search area with radius equal to the average radius of a supergranule (approximately 1.35×10^4 km). Then, it computes the difference of the coordinates between the center of the area and the pixel with the largest value in the area. This difference is regarded as the movement of the attractor in a one-day time step as a result of diffusion processes because all the supergranular cells are initially assumed to have the same radius. In fact, the size is different for each cell. To make the situation more authentic, a Gaussian distribution with peak value of 1.0 and a range between 0.5 and 1.5 is multiplied. The diffusion processes are suppressed in active areas with strong magnetic fields. For pixels whose $|B| \ge 25$ G, the diffusion processes are neglected.

3.2 The prediction of $F_{10.7}$

We used two versions of the surface flux transport model (WH and Y) to imitate the variation of the 10.7 cm radio flux from 2003 to 2014. The data come from SOHO/MDI, SDO/HMI and GONG. To improve the precision of the prediction results, we separated the regression period from 2003 to 2014 into three intervals, i.e., a descending phase (2003.10–2006.12), a minimum phase (2007.01–2010.05) and an ascending phase (2010.06–2014.10) of solar activity. The longer the regression period is, the higher the coefficient index will be. We used the same data sources in the same period, and the data were not merged together. We used the HMI magnetograms from June 2010 to October 2014, and mainly the MDI data from October 2003 to May 2010, except for the data gap. For example, there are several days in a year for which the MDI has no data, and we used the magnetograms from GONE to fill the gaps. We should consider the calibrations when combining different data sources, but because only several days in a year were involved, we ignored this difference.

The empirical formula associated with the 10.7 cm flux is as follows:

$$F_{model} = m_0 + m_1 S_P + m_2 S_A \tag{6}$$

$$S_P = \frac{1}{\sum \omega_\theta} \sum_{50\,\mathrm{G}<|B_r|}^{|B_r|<200\,\mathrm{G}} |B_r|\omega_\theta \tag{7}$$

$$S_A = \frac{1}{\sum \omega_\theta} \sum_{200\,\mathrm{G}\le|B_r|} |B_r|\omega_\theta \tag{8}$$

Where ω_θ is the weight of the solar surface area corresponding to its latitude, S_P is the sum of the magnetic fields where $50\ \mathrm{G} < |B_r| < 200$ G, and S_A is the sum of the magnetic fields where $|B_r| \ge 200$ G. The coefficients of m_0, m_1 and m_2 can be calculated by the REGRESS function in IDL

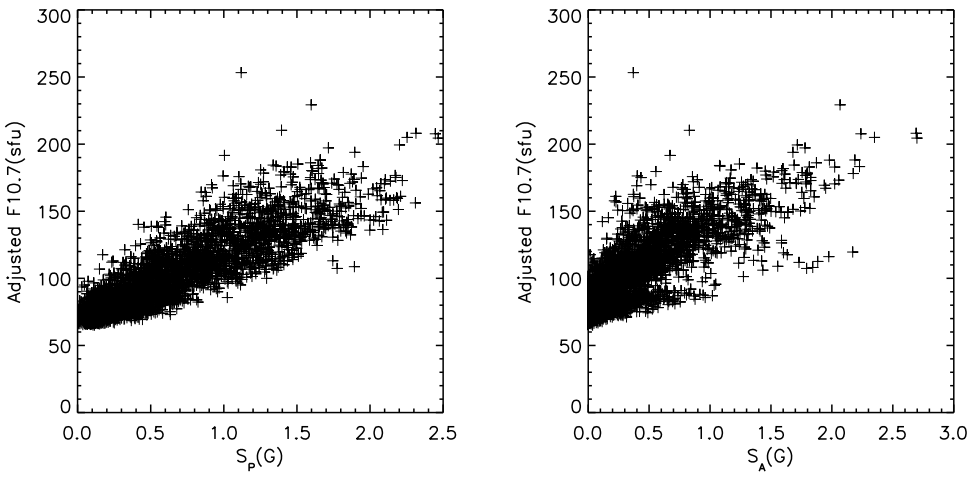

Fig. 1 Scatter plot of the observed $F_{10.7}$ relative to the plage index S_P (magnetic absolute value between 50 G and 200 G) and the spot index S_A (magnetic absolute value greater than 200 G) from 2003 to 2014. The magnetic fields come from the radial magnetograms that were input into the SFT model

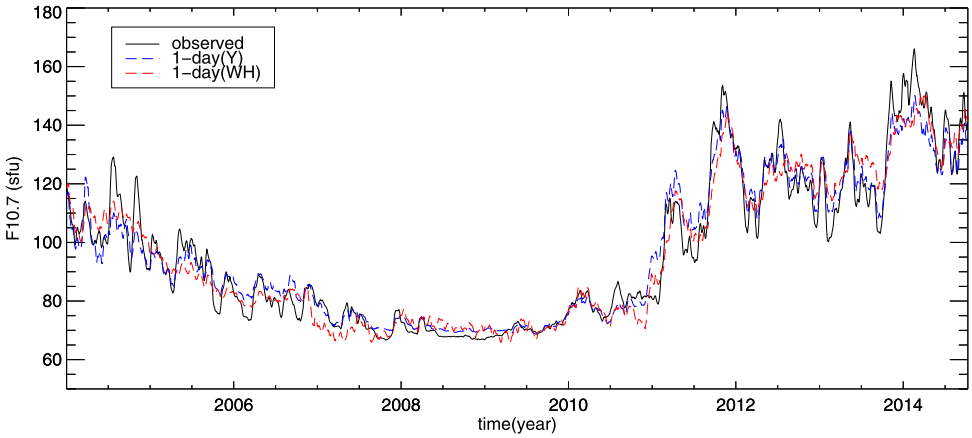

Fig. 2 Comparison of the observed $F_{10.7}$ values (black solid line) and the results of the 1-day forecasts using the WH (red dashed line) and Y (blue dashed line) flux transport models. The 27-day running-mean method was used for 11 years of data

if we provide the S_A, S_P and observed $F_{10.7}$ values. The magnetic field in the formula is the Earth-side radial magnetic field produced by the SFT model. The number of grids was 180 in latitude and 180 in longitude.

4 Results and discussions

To find the relationship between the two parameters (S_P and & S_A) and $F_{10.7}$, we show the scatter plots between them (Fig. 1). From the results, we found a good positive correlation between the $F_{10.7}$ index and the two parameters. As S_P and S_A increase, the value of $F_{10.7}$ grows as well.

We applied two versions of the solar magnetic flux transport model to modify the magnetic evolution of the photosphere from 2003 to 2014. We predicted the values of the $F_{10.7}$ 1 day and 3 days in advance and compared the predictions with the adjusted data. From Figs. 2 and 3, we note that the fitting results are close to the observed values in general. During the periods of solar maximum, the predicted values display larger deviations and lag effects than during those of solar minimum. Because the back side of the Sun cannot be observed, and because there is an angle between the plane of the ecliptic and the Sun's equator, foreshortening effects leading to the evolution of the magnetograms cannot reflect the real magnetic conditions on the solar surface. However, the results of the WH model show a small delay over the Y model, possibly because it neglects diffusion effects in the regions where magnetic fields are stronger than 25 G. During the solar minimum, $F_{10.7}$ undergoes a smooth variation, and the forecasting results are closer to the observed values.

Table 1 presents the statistic coefficients between the observed data and the 1- and 3-day forecast estimates using

Table 1 Comparison between the observed data and the estimated 1-day and 3-day forecast values using the WH and Y flux transport models from 2003 to 2014

Model	Forecast days	Spearman coefficients	Pearson coefficients	Average absolute value error	Root mean square error
WH	1	0.94	0.96	5.38	7.29
Y		0.98	0.98	3.38	5.56
WH	3	0.94	0.95	5.86	7.93
Y		0.98	0.97	4.12	6.13

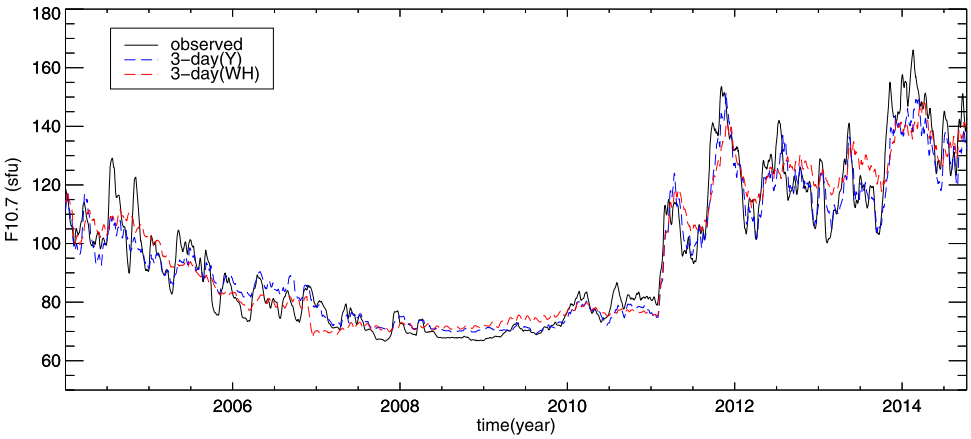

Fig. 3 Comparison of the observed $F_{10.7}$ values (black solid line) and the results of the 3-day forecasts using the WH (red dashed line) and Y (blue dashed line) flux transport models. The 27-day running-mean method was used for 11 years of data

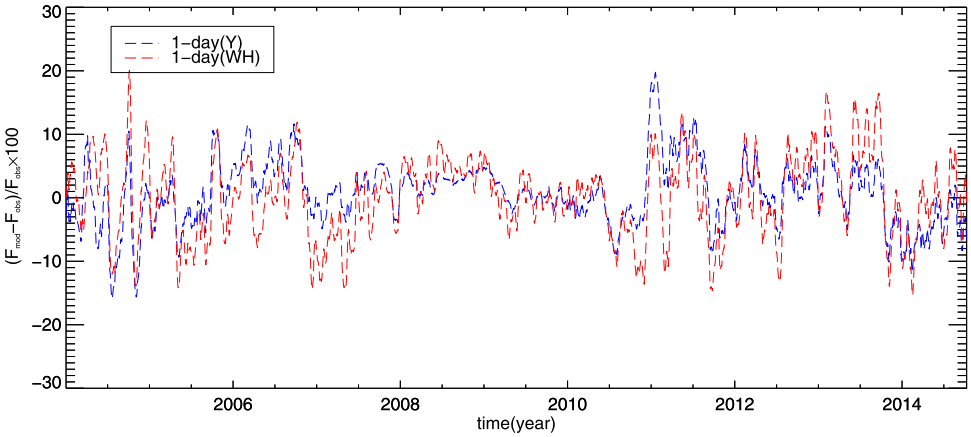

Fig. 4 Comparison of the relative errors between the observed $F_{10.7}$ values and the results of the 1-day forecasts using the WH (red dashed line) and Y (blue dashed line) flux transport models. The 27-day running-mean method was used for 11 years of data

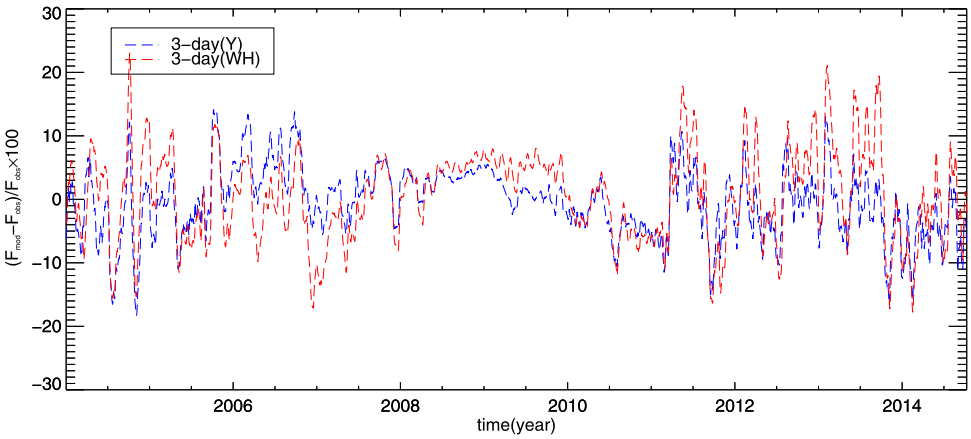

Fig. 5 Comparison of the relative errors between the observed $F_{10.7}$ values and the results of the 3-day forecasts using the WH (red dashed line) and Y (blue dashed line) flux transport models. The 27-day running-mean method was used for 11 years of data

the WH and Y flux transport models. The results show that the Person coefficient of the Y model reached a high level, with values of 0.98 and 0.97 when estimated 1 and 3 days in advance, respectively, during the 11 years. The mean absolute error and root mean square error were also small during the 1-day forecast, 3.8 and 5.56, respectively. However, the performance of the WH model was slightly worse than the Y model. Its Pearson coefficients were 0.96 and 0.95 when forecast for 1 and 3 days, respectively. The mean absolute error and root mean square error were higher than the Y model.

Figures 4 and 5 show the relative errors between the predicted and the observed values when forecasting $F_{10.7}$ 1 day and 3 days in advance, respectively. From the results, we observe that the performance of the two models is affected by solar activity levels. During the solar maximum (for example, 2003–2006), the relative errors of both models are higher than those during the minimum. The relative error of

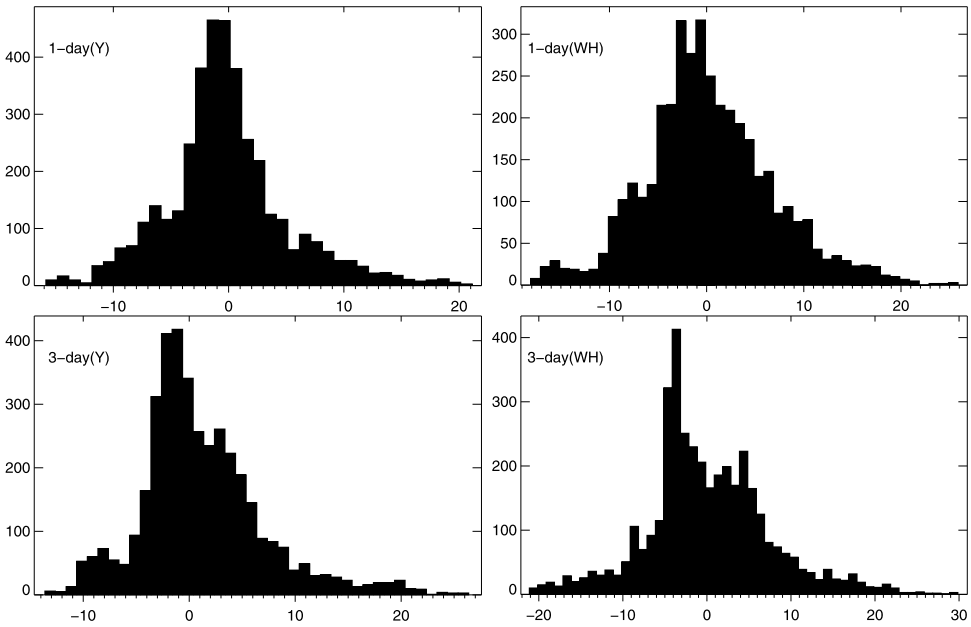

Fig. 6 Frequency diagram of the difference between the observed $F_{10.7}$ values and the model estimates. Left column represents the Y model, right column represents the WH model. The first and second rows represent 1-day and 3-day forecasts, respectively. Horizontal axis denotes $F_{obs} - F_{mod}$ (sfu)

the 1-day forecast of the Y model is below 15%, while those of the WH model are occasionally nearly 20%. During the solar minimum, both models perform well, with smaller relative error values, basically below 5%. While the results of the Y model are better than those of the WH model, we can conclude from the above analysis that the Y model is more suitable than the WH model to forecast $F_{10.7}$ during a solar maximum or minimum.

To investigate the distribution characteristics of the differences between the observed $F_{10.7}$ values and the model predictions, we plotted the frequency distribution, as shown in Fig. 6. In this figure, we note that the frequency distributions of both of the models present a nearly normal distribution with mean value of zero, although the error distributions of the Y model are more concentrated than those of the WH model for both the 1-day and 3-day forecasts.

The magnetic distributions produced by the SFT model depend on the selection of the parameters. The meridional flow in the WH is different from that in the Y model. To find a better parameter and investigate the performance of the forecast ability, we used the profile of Whitbread et al. (2017):

$$v(\theta) = -v_0 \sin^p \theta \cos\theta \tag{9}$$

where $v(\theta)$ is the meridional flow and θ is the colatitude. Both v_0 and p are free parameters to be optimized. Here, we select three types of the meridional flow profiles (Fig. 7), a) $v_0 = 15\ \mathrm{m\,s^{-1}}$, $p = 2$, b) $v_0 = 15\ \mathrm{m\,s^{-1}}$, $p = 10$, c) $v_0 = 11.3\ \mathrm{m\,s^{-1}}$, $p = 1.87$.

When using (9), we adopted the same meridional flow equation for both models to forecast the same number of days in advance. Table 2 shows the prediction performance

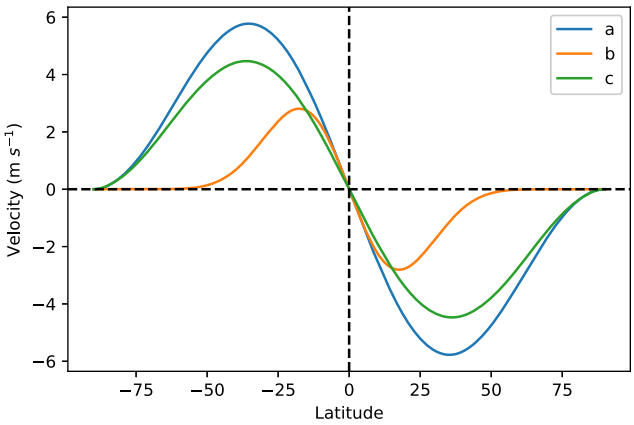

Fig. 7 Three types of meridional flow profiles in (9). a) $v_0 = 15\ \mathrm{m\,s^{-1}}$, $p = 2$, b) $v_0 = 15\ \mathrm{m\,s^{-1}}$, $p = 10$, c) $v_0 = 11.3\ \mathrm{m\,s^{-1}}$, $p = 1.87$

of the two SFT models. The statistical parameters of the Y model are better than those of the WH model for the same forecast days. For the same equation, the Y model performs better than the WH model. Therefore, the Y model is more robust in prediction of $F_{10.7}$ values when using different meridional flow profiles.

5 Conclusions

We employed two solar surface flux transport models to estimate the magnetic field of the Sun and to forecast the value of 10.7 cm flux. The fitting results are close to the observed values of $F_{10.7}$, except during violent solar periods. These methods can be used to forecast short-term variations of the $F_{10.7}$.

Table 2 The performances of the WH and Y models with different types of meridional flows

Model	Forecast days	Spearman coefficients	Pearson coefficients	Average absolute value error	Root mean square error	Meridional flow
WH	1	0.97	0.96	4.83	6.93	a
Y		0.98	0.98	4.02	5.76	
WH	3	0.96	0.96	5.28	7.67	a
Y		0.98	0.97	4.78	6.78	
WH	1	0.97	0.96	4.88	7.08	b
Y		0.98	0.98	4.01	5.76	
WH	3	0.96	0.95	5.44	7.87	b
Y		0.98	0.97	4.77	6.78	
WH	1	0.97	0.96	4.75	6.92	c
Y		0.98	0.98	4.02	5.76	
WH	3	0.96	0.96	5.37	7.69	c
Y		0.98	0.97	4.78	6.78	

In our simulations, we investigated the coefficient of correlation, mean absolute error, root mean square error and frequency distribution between the fitting results and the observed values. The performance of the Y model was better than the WH model. Hickmann et al. (2015) pointed out that the meridional flow in the WH model does not match observations, especially at lower latitudes. According to Mackay and Van Ballegooijen (2006), the meridional term used in the Y model was determined by the observations. We then applied different meridional flow profiles to both models to predict the $F_{10.7}$ values. The prediction of the Y model was more consistent with observations. Therefore, we conclude that the Y model is more suitable to forecast $F_{10.7}$ values. The supergranular diffusion is difficult to measure directly. In the SFT models, it is described as a random walk process or a diffusion coefficient. In fact, the supergranular flows are suppressed by strong sunspots and plage fields in the active regions (Wang 2017; Mackay and Yeates 2012). In the WH model, the author simply shut off diffusion in regions of magnetic field strength greater than 25 G. This is a crude method that will overestimate the global magnetic flux, as pointed out by Hickmann et al. (2015).

The solar flux transport model can modify the large-scale activities of solar magnetic fields. However, local variations cannot be considered. Therefore, the magnetic fields produced by this model differ in details compared with the real magnetic surroundings. These cause difficulties in predicting the $F_{10.7}$ exactly.

During the periods of the solar maximum, both models have a larger difference between the predicted and observed values. Many phenomena on the Sun are associated with $F_{10.7}$. The magnetic field is one of the important factors. We will consider other variables and improve the empirical formula in our future work.

References

Ahluwalia, H.S.: Adv. Space Res. **57**(2), 710 (2016). https://doi.org/10.1016/j.asr.2015.11.015

Akhmedov, S.B., Borovik, V., Gelfreikh, G., Bogod, V., Korzhavin, A., Petrov, Z., Dikij, V., Lang, K.R., Willson, R.F.: Astrophys. J. **301**, 460 (1986)

Baumann, I., Schmitt, D., Schüssler, M., Solanki, S.: Astron. Astrophys. **426**(3), 1075 (2004)

Bilitza, D.: Radio Sci. **36**(2), 261 (2001). https://doi.org/10.1029/2000RS002432

Chapman, G.A., Boyden, J.E.: Astrophys. J. Lett. **302**, 71 (1986). https://doi.org/10.1086/184640

Chatterjee, T.N.: Mon. Not. R. Astron. Soc. **323**(1), 101 (2001). https://doi.org/10.1046/j.1365-8711.2001.04110.x

Chen, Y., Liu, L., Le, H., Wan, W.: J. Geophys. Res. (2018). https://doi.org/10.1002/2017JA024765

Choudhuri, A.R., Chatterjee, P., Jiang, J.: Phys. Rev. Lett. **98**(13), 131103 (2007). https://doi.org/10.1103/physrevlett.98.131103

Courant, R., Friedrichs, K., Lewy, H.: IBM J. Res. Dev. **11**(2), 215 (1967). https://doi.org/10.1147/rd.112.0215

Dikpati, M., Gilman, P.A.: Space Sci. Rev. **144**(1), 67 (2009). https://doi.org/10.1007/s11214-008-9484-3

Dikpati, M., De Toma, G., Gilman, P.A.: Geophys. Res. Lett. **33**(5), L05102 (2006). https://doi.org/10.1029/2005gl025221

Gary, D.E., Hurford, G.: Astrophys. J. **317**, 522 (1987)

Henney, C.J., Toussaint, W.A., White, S.M., Arge, C.N.: Space Weather **10**(2), S02011 (2012). https://doi.org/10.1029/2011SW000748

Henney, C.J., Hock, R.A., Schooley, A.K., Toussaint, W.A., White, S.M., Arge, C.N.: Space Weather **13**(3), 141 (2015). https://doi.org/10.1002/2014SW001118

Hickmann, K.S., Godinez, H.C., Henney, C.J., Arge, C.N.: Sol. Phys. **290**(4), 1105 (2015)

Hotta, H., Yokoyama, T.: Astrophys. J. **709**(2), 1009 (2010). https://doi.org/10.1088/0004-637x/709/2/1009
Huang, C., Liu, D.-D., Wang, J.-S.: Res. Astron. Astrophys. **9**(6), 694 (2009). https://doi.org/10.1088/1674-4527/9/6/008
Jain, K., Hasan, S.S.: Astron. Astrophys. **425**(1), 301 (2004). https://doi.org/10.1051/0004-6361:20047102
Kholikov, S., Serebryanskiy, A., Jackiewicz, J.: Astrophys. J. **784**(2), 145 (2014). https://doi.org/10.1088/0004-637x/784/2/145
Kosovichev, A.G.: Space Sci. Rev. **144**(1), 175 (2009). https://doi.org/10.1007/s11214-009-9487-8
Krivova, N.A., Solanki, S.K., Wenzler, T., Podlipnik, B.: J. Geophys. Res., Atmos. **114**(D1), D00I04 (2009). https://doi.org/10.1029/2009JD012375
Lampropoulos, G., Mavromichalaki, H., Tritakis, V.: Sol. Phys. **291**(3), 989 (2016). https://doi.org/10.1007/s11207-016-0859-4
Leighton, R.B.: Astrophys. J. **140**, 1547 (1964). https://doi.org/10.1086/148058
Mackay, D., Van Ballegooijen, A.: Astrophys. J. **641**(1), 577 (2006)
Mackay, D.H., Yeates, A.R.: Living Rev. Sol. Phys. **9**(1), 6 (2012). https://doi.org/10.12942/lrsp-2012-6
Parker, D.G., Ulrich, R.K., Pap, J.M.: Sol. Phys. **177**(1), 229 (1998). https://doi.org/10.1023/A:1005050108870
Snodgrass, H.B.: Astrophys. J. **270**(1), 288 (1983). https://doi.org/10.1086/161121
Svalgaard, L.: Sol. Phys. **291**(9), 2981 (2016). https://doi.org/10.1007/s11207-016-0921-2
Tapping, K.F.: Space Weather **11**(7), 394 (2013). https://doi.org/10.1002/swe.20064
Tapping, K., DeTracey, B.: Sol. Phys. **127**(2), 321 (1990)
Virtanen, I., Virtanen, I., Pevtsov, A., Yeates, A., Mursula, K.: Astron. Astrophys. **604**, 8 (2017)
Wang, Y.-M.: Space Sci. Rev. **210**(1–4), 351 (2017)
Whitbread, T., Yeates, A., Muñoz-Jaramillo, A., Petrie, G.: Astron. Astrophys. **607**, 76 (2017)
Worden, J., Harvey, J.: Sol. Phys. **195**(2), 247 (2000). https://doi.org/10.1023/A:1005272502885
Yeates, A.R., Mackay, D.H., van Ballegooijen, A.A.: Sol. Phys. **245**(1), 87 (2007). https://doi.org/10.1007/s11207-007-9013-7
Yeates, A.R., Nandy, D., Mackay, D.H.: Astrophys. J. **673**(1), 544 (2008). https://doi.org/10.1086/524352
Zhao, J., Han, Y.-B.: Chin. J. Astron. Astrophys. **8**(4), 472 (2008)